1992

Comparison of Heat-Fin Materials and Design of a Common-Pressure-Vessel Nickel-Hydrogen Battery

Junbom Kim
Texas A & M University - College Station

Ralph E. White
University of South Carolina - Columbia, white@cec.sc.edu

Publication Info

Journal of the Electrochemical Society, 1992, pages 3492-3499.

http://dx.doi.org/10.1149/1.2069105
DOI: 10.1149/1.2069105

The reversibility of the octanoate adsorption was assessed by stepping the potential from –1 to +1 V *vs.* SHE (positive sweep), and then back from +1 to –1 V (negative sweep), and measuring friction and inverse capacitance for a 0.1 w/o solution of octanoic acid (Fig. 8). Friction and capacitance displayed hysteresis between the sweeps, though both returned to a value near the original at the end of the negative sweep, indicating desorption of the octanoate film.

Conclusion

Static friction, current, capacitance, and radiotracer measurements have all shown the potential-dependent nature of lubricant-film formation in aqueous solutions of octanoic acid neutralized with sodium hydroxide. In a solution of 1 w/o octanoic acid, the static coefficient of friction between mild steel and iron was reduced by more than 50% on changing the electrode potential from –400 to 300 mV *vs.* SHE. This may be due to electrostatic interactions between negatively charged octanoate species and the electrode; at potentials above the pzc of iron (*ca.* –400 mV *vs.* SHE), the electrode is positively charged, enabling the adsorption of a lubricating octanoate film. At potentials below –400 mV *vs.* SHE, film formation was inhibited, and friction consequently increased.

Acknowledgment

The authors thank Peter Bird and Peter Leyland for useful discussions on aqueous lubricants, Drew McMahon for advice on radiotracer studies, and Celina Jessop for the BET measurement. Permission to publish this paper has been granted by the British Petroleum company PLC.

Manuscript submitted April 30, 1992; revised manuscript received July 21, 1992.

REFERENCES

1. T. Edison, *Teleg. J.*, **5**, 189 (1877); *ibid.*, **7**, 332 (1879).
2. K. R. Koch, *Weid. Ann.*, **7**, 92 (1879).
3. M. K. Waitz, *ibid.*, **20**, 285 (1883).
4. F. P. Bowden and L. Young, *Research*, **3**, 235 (1950).
5. J. O'M. Bockris and R. Parry-Jones, *Nature*, **171**, May 23rd (1953).
6. J. O'M. Bockris, S. D. Argade, and E. Gileadi, *Electrochim. Acta*, **14**, 1259 (1969).
7. S. N. Postnikov, *Electrophysical and Electrochemical Phenomena in Friction, Cutting and Lubrication*, Van Nostrand, New York (1979).
8. B. B. Damaskin, O. A. Petrii, and V. V. Batrakov, in *Adsorption of Organic Compounds on Electrodes*, Chap. 7, Plenum, New York (1971).
9. G. Horanyi, *Electrochim. Acta*, **35**(6), 919 (1990).
10. A. J. McMahon, *Colloids and Surfaces*, **59**, 187 (1991).
11. E. H. Pryde, *Fatty Acids*, AOCS (1979).
12. T. N. Voropaeva, B. V. Deyagin, and B. N. Kabanov, *Izv. Akad. Nauk. SSSR*, 257 (1963).
13. E. O. Ayazyan, *Dokl. Akad. Nauk. SSSR*, **100**, 473 (1955).
14. F. P. Bowden and D. Tabor, *The Friction and Lubrication of Solids*, Clarendon Press, Oxford (1950).
15. K. S. Markley, *Fatty Acids. Their Chemistry, Properties, Production, and Uses. Part 1*, Interscience, New York (1960).

Comparison of Heat-Fin Materials and Design of a Common-Pressure-Vessel Nickel-Hydrogen Battery

Junbom Kim* and R. E. White**

Center for Electrochemical Engineering, Department of Chemical Engineering, Texas A&M University, College Station, Texas 77843

ABSTRACT

A two-dimensional, axisymmetric, and time-dependent thermal model was developed to study the temperature behavior of the cylindrically shaped common-pressure-vessel nickel-hydrogen cell. A differential-energy-balance equation was used as the governing equation. A finite-element software package called PDE/Protran was used to solve this model. Different materials such as copper, copper beryllium, silver, and sterling silver were compared as heat-fin materials. The heat-fin geometry (thickness and height) and spacing were tested to find a design that yielded an acceptable temperature gradient inside a nickel-hydrogen cell. Pulse heat-generation rates were tested and correlated with the time-dependent heat-generation cases.

A nickel-hydrogen battery is used extensively as an energy storage system in satellite applications due to its distinctive characteristics such as long cycle life, high energy density, and tolerance to overcharge.[1,2] A common-pressure-vessel nickel-hydrogen battery consists of several cell stacks within one common pressure vessel. Recently, this system has attracted attention because of its improved characteristics compared to the individual-pressure-vessel nickel-hydrogen battery such as higher energy density, lower manufacturing cost, and longer life expectancy.[3-5] However, common-pressure-vessel design has disadvantages to overcome such as electrolyte-management and thermal-control problems.[3,6] Polyethylene-cell encasement is used to solve the electrolyte-management problem.[7] Heat is absorbed at the beginning of the charge and released at the end of the charge and during discharge.[8-10] The main reaction of hydrogen formation and consumption does not cause a thermal-control problem. However, the side reaction produces oxygen, and much heat is released when oxygen is recombined with hydrogen.[11-13] A metal fin is inserted between the cells to remove the heat produced inside the cell during the cell reaction. An important physical characteristic in choosing the heat-fin material is the thermal diffusivity. The materials which have high thermal diffusivity values are silver, gold, copper, and aluminum.[14] Gold and aluminum are excluded from testing as heat-fin materials because gold is too expensive and aluminum is not chemically stable in the environment of the potassium hydroxide electrolyte. Silver, copper, and their alloys such as sterling silver and copper beryllium are compared as heat-fin materials.

Model Formulation

The back-to-back-design nickel-hydrogen battery is used in this modeling work as shown in Fig. 1a. One module consists of nine layers of cell-stack materials: two diffusion screens, two negative electrodes, two separators, two positive electrodes, and an absorber. Polyethylene encasement is used as the cell container to manage the problem of elec-

* Electrochemical Society Student Member.
** Electrochemical Soceity Active Member.

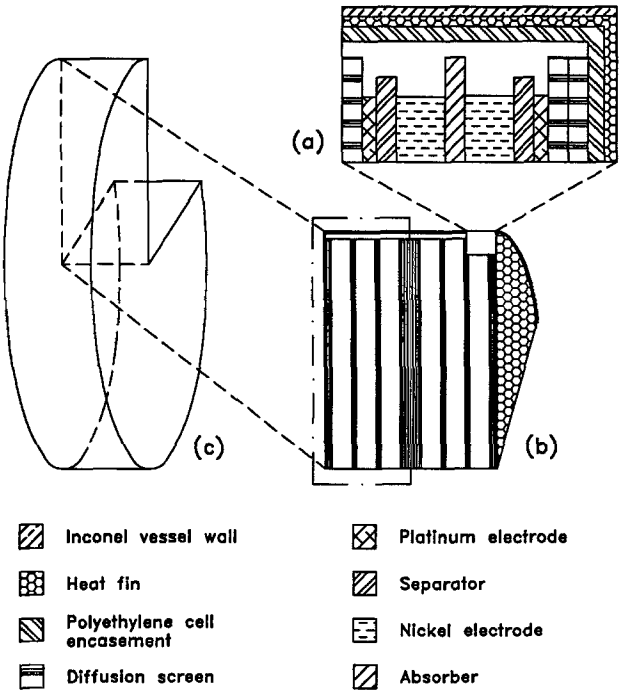

Fig. 1. Schematic representation of the nickel-hydrogen cell: (a) module and cell casing, (b, c) cylindrically shaped cell stack.

trolyte bridging between cells.[3,15] One cell consists of three modules and is enclosed by cell encasement in the modeling work of this research, unless otherwise specified. There are two cells between the metal heat fins as shown in Fig. 1b. Due to symmetry, the modeled region is the left half of Fig. 1b, which is enclosed by the dashdot lines.

Potassium hydroxide solution of 26% concentration is used as the electrolyte, unless otherwise specified. A polypropylene screen is used as the diffusion layer, and its void region is assumed to be filled with hydrogen. The absorber, also called the reservoir, acts as the electrolyte supply to avoid local nickel-electrode electrolyte depletion due to temperature gradients or electrode expansion. Grafted polypropylene is used as the absorber layer, and its void region is assumed to be filled with electrolyte. Asbestos is used as the separator material. The void regions of the separator and nickel electrode are assumed to be filled with electrolyte. The void region of the platinum electrode is assumed to be filled with hydrogen. Four different materials, copper, copper beryllium, silver, and sterling silver are compared as heat-fin material. Inconel 718 is used as the pressure-vessel wall material.

Conduction is regarded as the heat-transfer mechanism inside the cell. A differential energy balance equation is applied in this conduction heat-transfer system

$$\rho_i c_{p,i} \frac{\partial T}{\partial t} = \nabla \cdot (\lambda_i \nabla T) + \dot{q}_i \qquad [1]$$

where ρ_i, $c_{p,i}$, λ_i, and $\dot{q}_i$ are the density, specific heat, thermal conductivity, and heat generation rates in region i, respectively. T and t are temperature and time, respectively. A cylindrically shaped cell stack of Johnson Controls' 11 A-h common-pressure-vessel nickel-hydrogen battery is modeled in this research as shown in Fig. 1c. Thus, for the axisymmetric case, a differential energy balance equation is used as the governing equation for region i of the system as follows

$$\rho_i c_{p,i} \frac{\partial T}{\partial t} = \lambda_i \left\{ \frac{1}{r} \frac{\partial}{\partial r} \left(r \frac{\partial T}{\partial r} \right) + \frac{\partial^2 T}{\partial^2 z} \right\} + \dot{q}_i \qquad [2]$$

where r and z are the radial and axial direction, respectively.

The effects of module component material porosities and potassium hydroxide electrolyte concentrations on the maximum cell temperature are investigated. The effectiveness of the heat-fin geometry in reducing the temperature gradient inside the cell is tested with a height and thickness variation using equal amounts of heat-fin material. Heat-fin spacing is compared using six and four modules between heat fins. Pulse shape heat-generation rate is correlated with the time-dependent heat-generation rates reported by Johnson Controls, Inc. (JCI).[7] Three different cases of modeling are studied: (*i*) steady state with constant heat-generation rate; (*ii*) unsteady state with pulse heat-generation rate; and (*iii*) unsteady state with heat generation rates reported by JCI.

A computer package called PDE/Protran[16] was used to solve Eq. 2 numerically by a finite-element method for the modeled region shown in Fig. 1b. The left and right sides of the modeled region are assumed to be adiabatic by symmetry because these are the center lines of repetition. The lower side of the modeled region is assumed to be adiabatic because this is the center line of the axisymmetric modeled region. The upper side of the modeled region is assumed to have a constant temperature of 10°C because this side is kept at constant temperature by thermal control.[4,17,18]

The thermal and physical properties such as thermal conductivity, density, and specific heat are averaged for each region i using the following equations

$$\lambda_i = \lambda_m (1 - \varepsilon) + \lambda_f \varepsilon \qquad [3]$$

$$\rho_i = \rho_m (1 - \varepsilon) + \rho_f \varepsilon \qquad [4]$$

$$c_{p,i} = c_{p,m} (1 - \varepsilon) + c_{p,f} \varepsilon \qquad [5]$$

where ε is the porosity value, and subscripts m, f, and i represent the values of the structural material, filling material, and calculated value with Eq. 3-5 of region i, respectively. The thermal conductivity values of the structural and filling materials are shown in Table I. The porosity values of the diffusion screen, platinum electrode, separator, nickel electrode, and absorber have been estimated.[11,19] Two different groups of porosity values are shown in parenthesis in Table II. The physical and thermal properties of each cell region are shown in Table III. These values are the averaged values using Eq. 3-5 with the group II porosity values of Table II and 26% potassium hydroxide electrolyte.

The maximum temperature difference allowed inside the cell to avoid the water relocation problem is calculated using the equation suggested by Kim *et al.*[11] as follows

$$\Delta T = 2.94872426 - 0.24737596W + 0.01376840W^2 + (0.01016541 - 0.00021840W + 5.04845 \times 10^{-5} W^2) T_c \qquad [6]$$

Table I. Thermal conductivity values of module component structural and filling materials.

Material	Thermal conductivity (W/cm · K)
Polyethylene encasement, λ_m	3.287×10^{-3}
Diffusion screen, λ_m	1.384×10^{-3}
Platinum electrode, λ_m	7.410×10^{-2}
Separator, λ_m	1.443×10^{-3}
Nickel electrode, λ_m	4.256×10^{-1}
Absorber, λ_m	1.384×10^{-3}
26% KOH, λ_f	5.723×10^{-3}
30% KOH, λ_f	5.665×10^{-3}
Hydrogen, λ_f	1.722×10^{-3}

Table II. Thermal conductivity groups for two different porosities and potassium hydroxide electrolyte concentrations, $\lambda_i(\varepsilon)$.

Material	Group I 30% KOH	Group II 26% KOH
Diffusion screen	1.553×10^{-3} (0.5)	1.654×10^{-3} (0.8)
Platinum electrode	3.988×10^{-2} (0.5)	3.357×10^{-2} (0.56)
Separator	4.821×10^{-3} (0.8)	4.353×10^{-3} (0.68)
Nickel electrode	2.534×10^{-1} (0.41)	2.535×10^{-1} (0.41)
Absorber	4.809×10^{-3} (0.8)	4.855×10^{-3} (0.8)

Table III. Physical and thermal properties.

Material	Density ρ_i (g/cm^3)	Thermal conductivity λ_i (W/cm · K)	Specific heat $c_{p,i}$ (J/g · K)	Ref.
Polyethylene encasement	9.30×10^{-1}	3.287×10^{-3}	2.301	7, 20
Vessel wall	8.193	1.470×10^{-1}	4.393×10^{-1}	7, 20
Copper beryllium	8.830	2.491	4.184×10^{-1}	20, 21
Copper	8.920	3.849	3.855×10^{-1}	20, 21
Sterling silver	10.408	3.620	2.463×10^{-1}	20, 21
Silver	10.490	4.028	2.350×10^{-1}	20, 21
Diffusion screen	1.829×10^{-1}	1.654×10^{-3}	11.828	19, 20, 21, 22
Platinum electrode	9.586×10^{-1}	3.357×10^{-2}	8.229	19, 20, 21, 23
Separator	1.635	4.353×10^{-3}	2.511	19, 20, 21, 23, 24
Nickel electrode	2.226	2.535×10^{-1}	1.560	19, 20, 21, 23
Absorber	1.181	4.855×10^{-3}	2.946	20, 21, 23

where ΔT, W, and T_c are the maximum temperature difference allowed, weight percent (w/o) of the potassium hydroxide solution, and the coldest point temperature in the nickel-hydrogen battery, respectively.

Results and Discussion

Two different cell-component material porosities and potassium hydroxide electrolyte concentrations (Table II), were tested for the maximum temperature inside the cell. The maximum temperature difference between the two groups is not significant (less than 0.95%). Thus, the estimated porosity values can be used in calculating the temperature gradient inside the cell without producing a significant error. Polyethylene and nylon are compared as cell encasement materials, and the maximum temperature difference between these two cases is not significant (less than 0.96%). Group II porosity values of Table II, 26% potassium hydroxide solution, and polyethylene cell encasement are used in the modeling of this research. The outside vessel wall temperature is assumed to be constant at 10°C, and the maximum temperature difference allowed inside the cell is 6.21°C according to Eq. 6.

Steady state with constant heat-generation rate.—The heat flows of the modeled region are represented by the vector plots as shown in Fig. 2. The modeled region without a heat fin is shown in Fig. 2a and with a heat fin is shown in Fig. 2b. A constant heat generation rate of 0.04 W/cm^3 and a copper beryllium heat fin of 0.03 cm thickness and 6 cm height are used for the steady-state case modeling, unless otherwise specified. The maximum temperature without a heat fin is 24.38°C on the lower-right corner of the modeled region and with a heat fin is 13.25°C on the same region as Fig. 2a. The vector size was modified to enhance the heat flow magnitude as shown in Fig. 2a, b. Actually, the vector size in Fig. 2b should be 16 times bigger than what is shown in the plot to compare with the vector size in Fig. 2a. As shown in Fig. 2b, most of the heat produced inside the cell is dissipated to the outside vessel wall through the heat fin, and the heat flow through the other region is not significant. The gap between the cell stack and vessel wall is small (less than 3 mm) and also partly occupied by the cell-encasement material. The temperature gradient in this region is not significant (less than 1°C). In these circumstances, viscous force overcomes buoyance force, and the heat transfer occurs by pure conduction.[14] Thus, the heat transfer by convection through the small gap between cell stack and vessel wall can be neglected. The heat transfer by radiation is also negligible compared to that of conduction because the temperature of the modeled region is between 10 and 20°C. Thus, it is reasonable to assume that conduction is the only mechanism of heat transfer in calculating the temperature behavior inside the cell without producing a significant error.

The heat-fin thickness is tested for different heat-fin materials as shown in Fig. 3. In this case, the heat-fin height is fixed at 6 cm. The maximum temperature difference between copper beryllium and silver is 0.85°C when the heat-fin thickness is 0.01 cm and 0.32°C when the heat-fin thickness is 0.06 cm. As the heat-fin thickness increases, the maximum temperature drop and the differences among the heat-fin materials becomes smaller because the other cell components become the major resistance to heat flow. The results of maximum temperature change with various heat-fin heights are shown in Fig. 4. In this case the heat-fin thickness is fixed at 0.03 cm. The temperature difference between copper beryllium and silver is 0.17°C when the heat-fin height is 1.0 cm and 0.50°C when the heat-fin height is 6.0 cm. As the heat-fin height increases, the maximum temperature difference between the materials becomes larger because the short fin does not remove heat sufficiently.

The efficient design (height and thickness) of the heat fin is tested for an equal amount of heat-fin material, and the results are shown in Fig. 5. Six different heat-fin heights are chosen, and each fin thickness is calculated to obtain equal amounts of heat-fin material. The dimensions of the heat-fin height and thickness are shown on the abscissa of

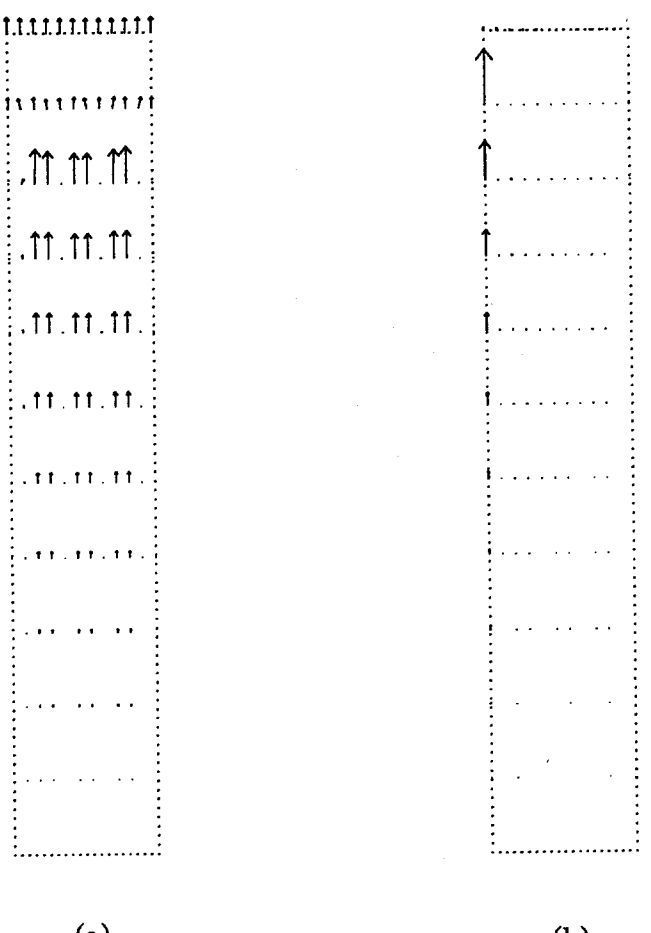

Fig. 2. Vector plots of the heat flow in the modeled region: (a) without heat fin, (b) with heat fin on the left side.

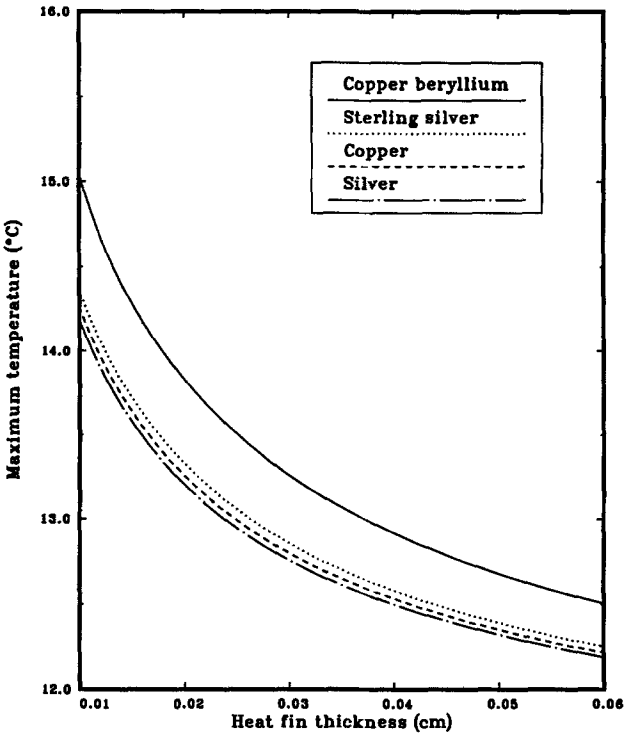

Fig. 3. Maximum temperatures for different heat-fin materials and thickness.

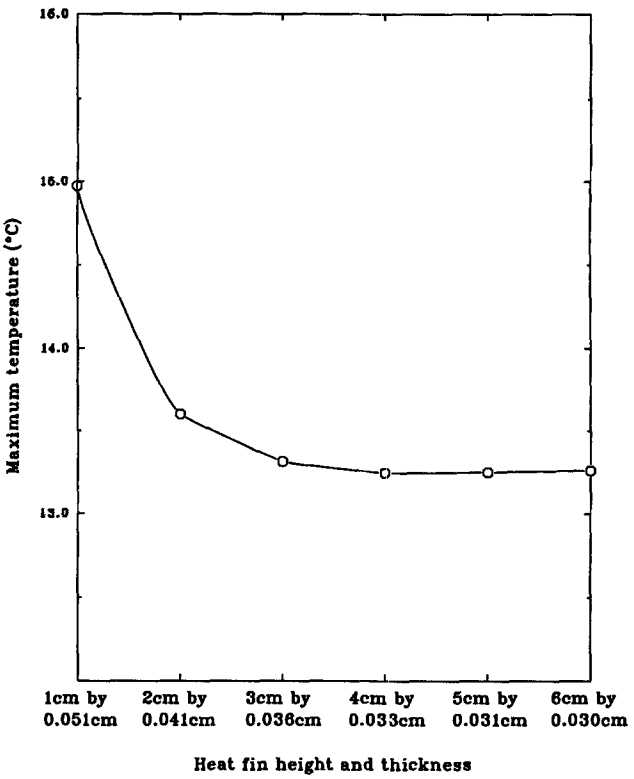

Fig. 5. The test of the efficient heat-fin dimension (height by thickness) for equal amounts of heat-fin material.

Fig. 5. The maximum temperatures are compared, and the lowest value occurred when a 4 cm by 0.033 cm heat fin is used. However, the maximum temperature difference between the 4 cm by 0.033 cm case and the 6 cm by 0.030 cm case is not significant (less than 0.51%). According to the results of Fig. 5, the doughnut-shaped heat fin, which is flat, and has a hole at the center, proved to be as efficient as the disk-shaped heat fin to remove the heat produced inside the cell when an equal amount of heat-fin material is used.

Unsteady state with pulse heat-generation rate.—Pulse heat generation rate is used to study the temperature response for unsteady state cases. The pulse heat-generation rate is shown as a solid line in Fig. 6, whose units are shown on the right-side ordinate. A copper beryllium heat-fin of a 0.03 cm thickness and 6.33 cm height is used for the unsteady state with the pulse heat generation unless otherwise specified. The maximum temperature, minimum temperature, and the temperature difference between the maximum temperature and minimum temperature are shown in Fig. 6, whose unit is shown on the left-side ordinate. The temperature contour plots of Fig. 6 at specific

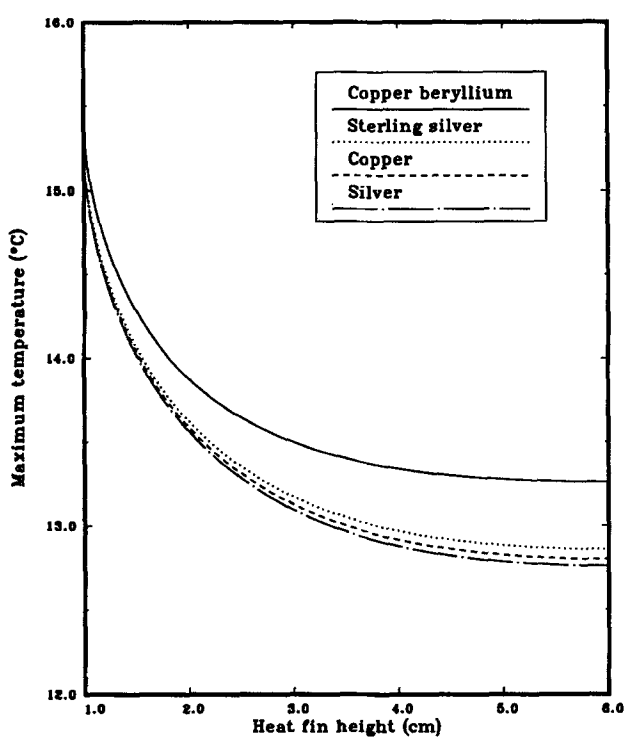

Fig. 4. Maximum temperatures for different heat-fin materials and height.

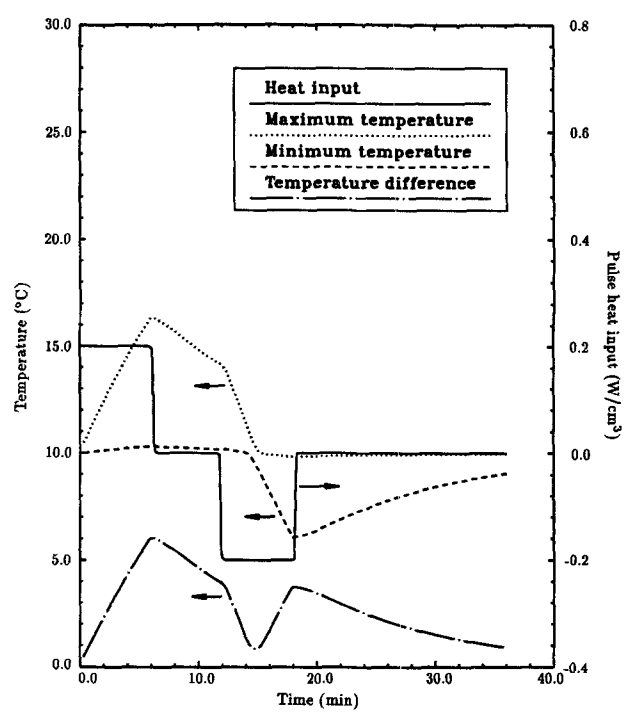

Fig. 6. Temperature response at unsteady state using pulse heat generation rate.

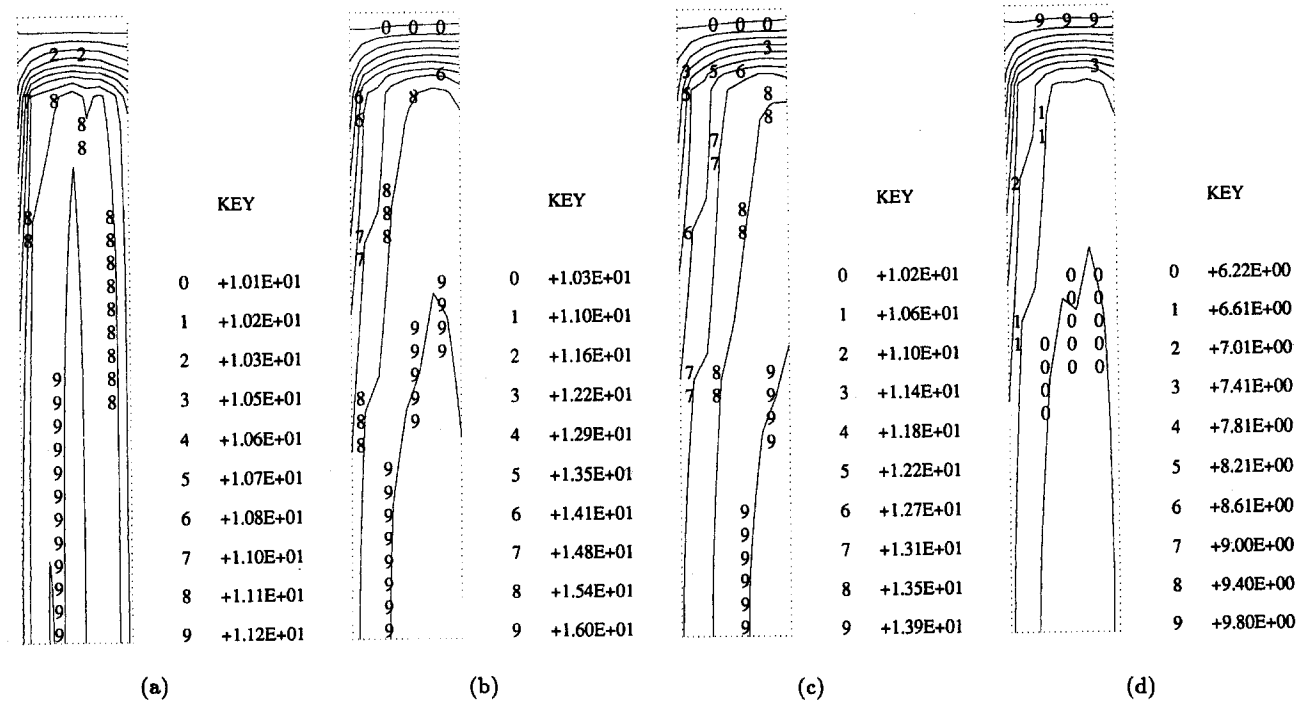

Fig. 7. Temperature contour plots of Fig. 6 at specific times: (a) 1 min, (b) 6 min, (c) 12 min, and (d) 18 min.

times are shown in Fig. 7, and the unit of the key number is °C. At the beginning of the positive heat generation (after 1 min), the maximum temperature occurs near the center of the three modules in the modeled region as shown in Fig. 7a. The temperature gradient did not develop much and there was not enough time to dissipate the heat produced inside the cell. After 6 min, the temperature gradient became steeper, and the heat produced inside the cell went towards the heat fin and then out to the vessel wall as shown in Fig. 7b. When the heat generation rate is negative (after 18 min) as shown in Fig. 7d, the shape of the contour lines appears similar to that of the Fig. 7b but with the gradient reversed.

The time-dependent heat-generation rates of a nickel-hydrogen battery of Johnson Controls, Inc., at the beginning of the life is shown in Fig. 8. The curve is based on a 55 min charge and 35 min, 40% depth of discharge for a low-earth-orbit regime.[7] It is assumed that the heat is generated uniformly, only on the nickel electrode, and this assumption has proved reasonable in calculating the temperature gradient inside the cell without producing significant errors as shown in the paper.[11] The magnitude of the heat-generation rates during the normal charge is not large, and the cell temperature during this period does not deviate much from the initial temperature of 10°C. The temperature increases rapidly during the overcharge, and the maximum temperature occurs at the end of the overcharge. The heat generation rate peak during overcharge is important in calculating the maximum temperature during a 90-min cycle.

The maximum temperature using the peak of the overcharge heat-generation-rate regime is different from that when using the whole 90-min cycle because of the temperature-gradient history before the overcharge regime. Pulse heat-generation rates are tested to be used instead of the heat-generation rates of Fig. 8. The heat-generation rates of the peak portion during the overcharge in Fig. 8 are averaged and compared with the pulse heat-generation rates as shown in Fig. 9. The maximum temperature difference of the pulse heat-generation rate of 0.196 W/cm^3 for 380 s is similar to that of JCI's as shown in Fig. 9. Thus, the pulse heat-generation rate of 0.196 W/cm^3 for 380 s is used in calculating the maximum temperature difference with different heat-fin thicknesses and materials, and the results are shown in Fig. 10. The maximum temperature difference using this pulse heat-generation rate is 0.06°C smaller than that when using JCI's. Thus, the corrected maximum temperature difference allowed is shown by line b of Fig. 10. As shown in Fig. 10, a 0.03-cm-thick sterling silver, copper, or silver, or a 0.04-cm-thick copper beryllium heat fin are alternatives to reduce the temperature gradient inside the cell to a value lower than the maximum temperature difference allowed to avoid the water relocation problem. Figure 11 shows the results using the same method as Fig. 10 except that four modules are used instead of six modules between heat fins. In this case, the maximum temperature difference of the pulse heat-generation rate of 0.206 W/cm^3 for 360 s is similar to that of JCI's, and it is

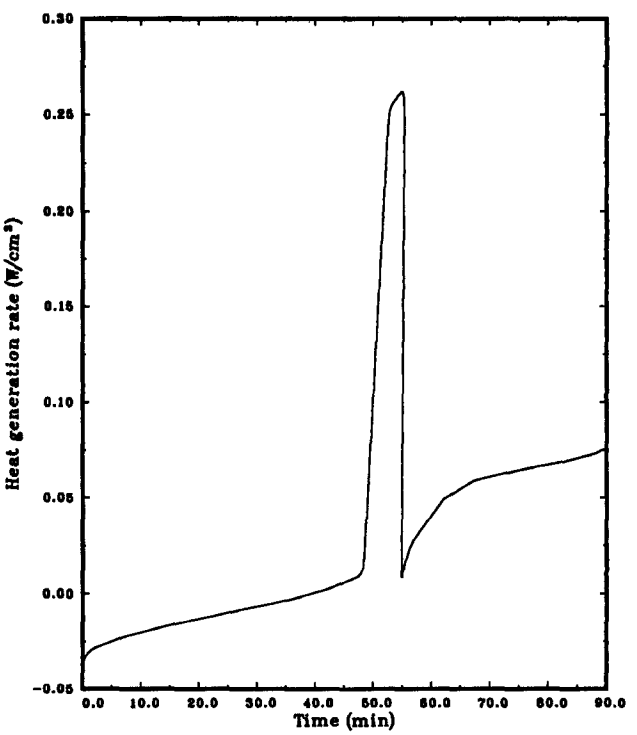

Fig. 8. Heat generation rates of JCI at the beginning of the life (55 min charge and 35 min, 40% depth of discharge for a low-earth-orbit regime).

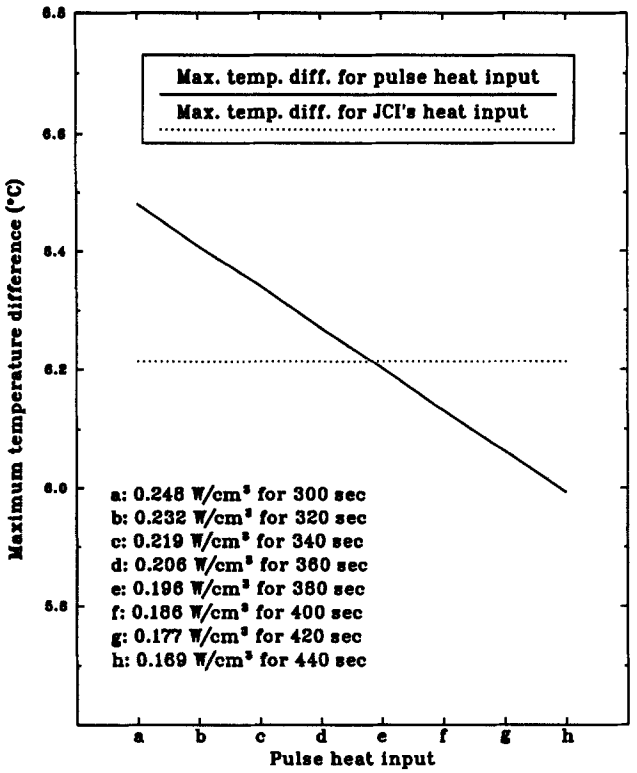

Fig. 9. Correlation of the pulse heat generation rate with JCI's when six modules between heat fins are used.

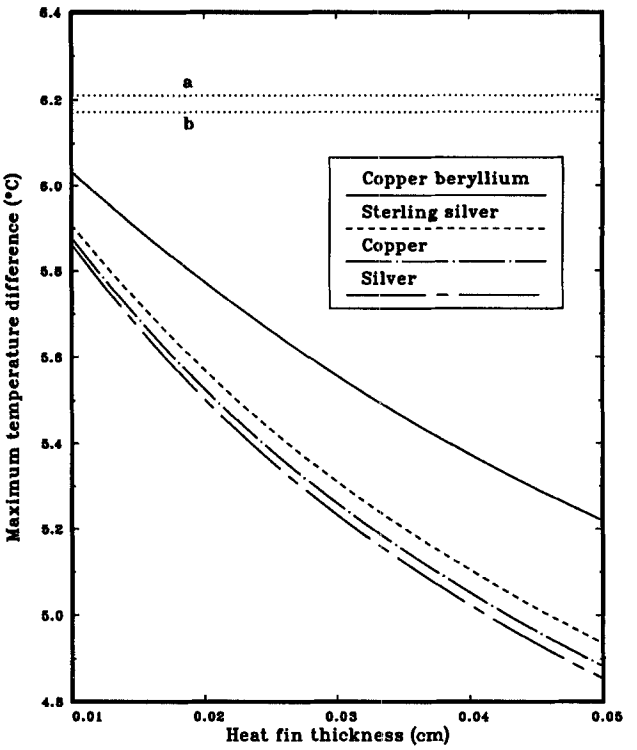

a : Maximum temperature difference allowed

b : Corrected maximum temperature difference allowed for pulse heat input

Fig. 11. Minimum heat-fin thickness needed for each heat-fin material to keep the temperature gradient inside the cell to a value lower than the maximum temperature difference allowed when four modules between heat fins are used.

used in calculating the values of Fig. 11. A 0.01-cm-thick copper beryllium, sterling silver, copper, or silver heat fin is sufficient to reduce the temperature gradient inside the cell to a value lower than the maximum temperature difference allowed.

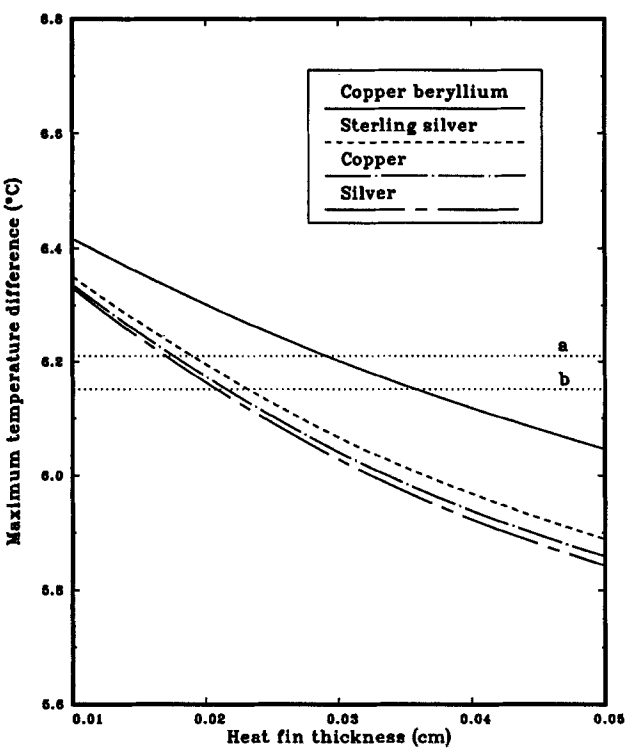

a : Maximum temperature difference allowed

b : Corrected maximum temperature difference allowed for pulse heat input

Fig. 10. Minimum heat-fin thickness needed for each heat-fin material to keep the temperature gradient inside the cell to a value lower than the maximum temperature difference allowed when six modules between heat fins are used.

Figure 12 shows the heat-fin-thickness correlation between six modules and four modules between heat fins. Each line represents the comparison of the heat-fin volume. As an example, a 0.04-cm-thick heat fin for a six-module case is equivalent to the 0.029-cm-thick heat fin for a four-module case. Thus, the results of the Fig. 10 and 11 can be summarized in Fig. 12. As shown in Fig. 12, the four-modules-between-heat fins array is preferred over the six-modules-between-heat-fins array to reduce the heat-fin volume by more than 50% when choosing copper beryllium, sterling silver, copper, or silver as fin material.

Unsteady state with the heat-generation rates reported by JCI.—According to the results of Fig. 12, four modules between heat fins and a copper beryllium heat fin of 0.01 cm thickness and 6.33 cm height are used in calculating the temperature behavior inside the cell. The heat generation rates of Fig. 8 are used during three repeating cycles, and only the maximum temperature difference inside the cell is shown in Fig. 13. The maximum temperature difference using copper beryllium is 6.04°C, sterling silver is 5.92°C, copper is 5.89°C, and silver is 5.87°C. Thus, a copper beryllium, sterling silver, copper, or silver heat fin of 0.01 cm thickness and 6.33 cm height is enough to keep the temperature gradient inside the cell to a value lower than the maximum temperature difference allowed (6.21°C) when the heat-generation rates reported by JCI and four modules between heat-fins are used.

Even though the temperature gradient inside the cell is a little higher than the maximum temperature difference allowed, the nickel-hydrogen cell has self-adjusting protection to prevent continuous water loss from the nickel electrode. As an example, in the case that the nickel electrode loses water due to temperature gradients and the potassium hydroxide electrolyte concentration changes from 26% to 27%, the maximum temperature difference allowed

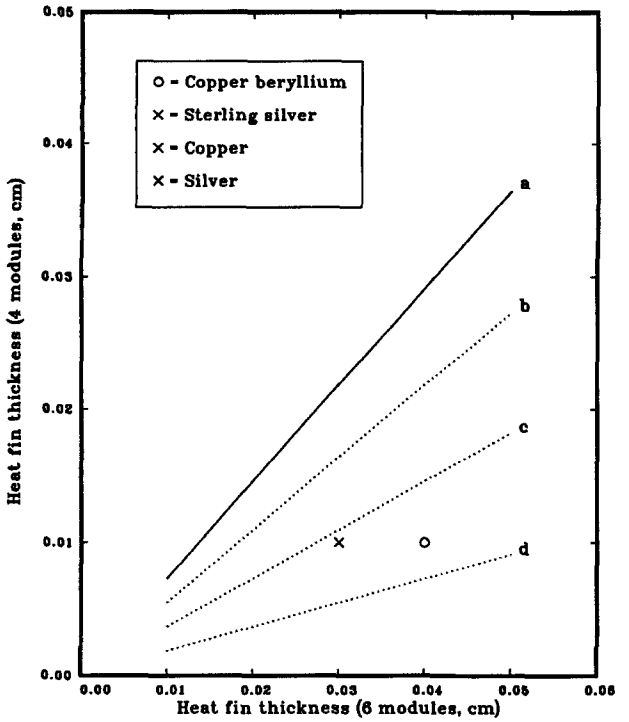

a : Equal heat fin volume between 6 modules and 4 modules
b : 25% heat fin volume reduction when using 4 modules
c : 50% heat fin volume reduction when using 4 modules
d : 75% heat fin volume reduction when using 4 modules

Fig. 12. Correlation of the minimum heat-fin thickness needed at each heat-fin material between six and four modules between heat fins.

changes from 6.21 to 6.72°C according to Eq. 6, and in turn this slows down or stops the water loss from the nickel electrode. Thus, the nickel-hydrogen cell can function properly as long as the maximum temperature difference inside the cell does not exceed significantly the maximum temperature difference allowed, even though the higher potassium hydroxide electrolyte concentration reduces the nickel-hydrogen-cell cycle life.

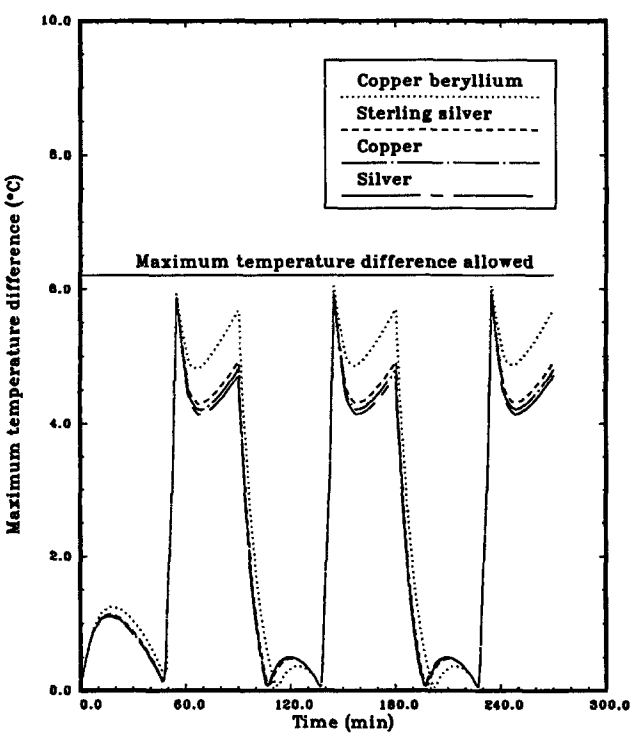

Fig. 13. Maximum temperature difference inside the cell when 0.01 cm thick and 6.33 cm high heat fin (copper beryllium, sterling silver, copper, or silver) and the heat-generation rates of Fig. 8 (three repeating cycles) are used.

Conclusion

The effects of the potassium hydroxide electrolyte concentrations and porosity values of the diffusion screen, platinum electrode, separator, nickel electrode, and absorber on the maximum cell temperature are not significant. Polyethylene and nylon are compared as cell encasement material, and there is no significant difference in maximum cell temperature. Most of the heat produced inside the cell can be dissipated to the outside vessel wall through a properly designed heat fin. A doughnut-shaped heat fin, which is flat with a hole at the center and made with equal amounts of material as a disk-shaped heat fin, can be as efficient as the disk-shaped heat-fin in reducing the temperature gradient inside the cylindrically shaped nickel-hydrogen cell.

When six modules are used between heat fins, a 0.03-cm-thick sterling silver, copper, or silver or a 0.04-cm-thick copper beryllium heat fin is a satisfactory alternative to reduce the temperature gradient inside the cell to a value lower than the maximum temperature difference allowed (6.21°C). When four modules are used between heat fins, a 0.01-cm-thick copper beryllium, sterling silver, copper, or a silver heat fin is sufficient to reduce the temperature gradient inside the cell to a value lower than the maximum temperature difference allowed. More than a 50% reduction in heat-fin material can be achieved by using four modules between heat fins compared to six modules betwen heat fins.

Manuscript submitted April 27, 1992; revised manuscript received Aug. 13, 1992.

Texas A&M University assisted in meeting the publication costs of this article.

LIST OF SYMBOLS

c_p specific heat, J/g · K
$c_{p,f}$ specific heat of filling material of porous region i, J/g · K
$c_{p,i}$ specific heat of region i including structural and filling material, J/g · K
$c_{p,m}$ specific heat of structural material of porous region i, J/g · K
$\dot{q}_i$ heat-generation rates of region i, W/cm^3
r radial direction
T temperature, °C
T_c the coldest point temperature in the nickel-hydrogen battery, °C
ΔT maximum temperature difference allowed in the nickel-hydrogen battery, °C
t time, s
W weight percent of potassium hydroxide solution
z axial direction

Greek symbols

ε porosity of region i
λ thermal conductivity, W/cm · K
λ_f thermal conductivity of filling material of porous region i, W/cm · K
λ_i thermal conductivity of region i including structural and filling material, W/cm · K
λ_m thermal conductivity of structural material of porous region i, W/cm · K
ρ density, g/cm^3
ρ_f density of filling material of porous region i, g/cm^3
ρ_i density of region i including structural and filling material, g/cm^3
ρ_m density of structural material of porous region i, g/cm^3

REFERENCES

1. G. F. Turner, *Astronautics and Aeronautics*, Nov., 18 (1975).
2. D. M. Allen, *Proceedings of the 31st Power Sources Symposium*, The Electrochemical Society, p. 49, Pennington, NJ (1984).

3. J. P. Žagrodnik and K. R. Jones, *Intersociety Energy Conversion Engineering Conference*, **6**, 85 (1990).
4. J. Brill, *NASA Aerospace Battery Workshop*, NASA Conference Publication 3119, 631 (1990).
5. L. Marcoux and J. K. Stedman, *Intersociety Energy Conversion Engineering Conference*, **1**, 555 (1984).
6. W. R. Scott, *ibid.*, **4**, 1453 (1983).
7. J. P. Zagrodnik, Personal communication.
8. A. G. Khotyaintsev, T. A. Molochnik, and B. I. Tsenter, *J. Appl. Chem. USSR*, **60** 1210 (1987).
9. A. Laursen, U. Fabricius, and P. Stangerup, NTIS N80-21882 (1979).
10. C. J. Johnson, in *Proceedings of the Symposium on Nickel Hydroxide Electrode*, D. A. Corrigan and A. H. Zimmerman, Editors, PV 90-4, p. 381, The Electrochemical Society Softbound Proceedings Series, Pennington, NJ (1990).
11. Junbom Kim, T. V. Nguyen, and R. E. White, Submitted to *This Journal*.
12. E. Buder, *J. Appl. Electrochem.*, **2**, 301 (1972).
13. E. Yeager and D. Tyrk, *Advances in Hydrogen Energy*, **2**, 827 (1984).
14. M. N. Özişik, *Heat Transfer*, McGraw-Hill Book Company, New York (1985).
15. G. L. Holleck, *Intersociety Energy Conversion Engineering Conference*, **3**, 1908 (1980).
16. *PDE/Protran User's Manual*, Ver. 2.0 (June 1989), IMSL, Houston, TX.
17. C. Bulle and A. Dupuy, NTIS 8928276 (1988).
18. S. N. Simons, B. C. Willhoite, and G. Ommering, NTIS 8924427 (1988).
19. R. L. Kerr, Ph.D. Dissertation, University of Dayton, Dayton, OH (1986).
20. R. H. Perry and C. H. Chilton, *Chemical Engineers Handbook*, 5th ed., McGraw-Hill, New York (1973).
21. J. A. Dean, *Lange's Handbook of Chemistry*, 13th ed., McGraw-Hill, New York (1985).
22. C. A. Schaeffer and G. Thodos, *Ind. Eng. Chem.*, **50**, 1585 (1958).
23. S. U. Falk and A. J. Salkind, *Alkaline Storage Batteries*, John Wiley and Sons, Inc., New York (1969).
24. R. C. Weast, *CRC Handbook of Chemistry and Physics*, 1st student ed., CRC Press, Inc., Boca Raton, FL (1988).

Enhanced-Surface-Area Packed-Bed Electrodes for Electrogenerative Oxidation of Sulfur Dioxide

Jongwook Lee* and Stanley H. Langer**

Department of Chemical Engineering, University of Wisconsin, Madison, Wisconsin 53706

ABSTRACT

Enhanced-surface-area packed-bed (ESAP) electrodes were designed and tested as anodes for aqueous SO_2 oxidation in electrogenerative SO_2/O_2 cells. They were prepared by attaching high-area carbon particles, with deposited platinum electrocatalyst, to larger graphite particles. The performance of ESAP electrodes was studied with various SO_2 concentrations (0.01 to 0.9*M*) in 3*M* H_2SO_4 at *ca.* 25°C and atmospheric pressure. The enhanced platinum area on the large-surface-area carbon led to significantly higher SO_2 oxidation rates. At all SO_2 concentrations, ESAP electrodes provided much higher current densities with higher cell voltages than did graphite sheet electrodes. The use of highly dispersed platinum (44% dispersion) without a significantly increased pressure-drop across the packed-bed is a major advantage of ESAP-type electrodes in special situations. The use of ESAP catalytic electrodes in our cell configuration did result in a slight bulk conductivity decrease, relative to a graphite sheet or particle, packed-bed electrode.

In earlier work involving the development of techniques for liquid-phase electrogenerative SO_2/O_2 cells,[1,2] graphite-sheet-supported platinum anodes were used initially because of their high conductivity, relatively inert character, and macroporosity for electrolyte flow, all requirements for liquid-phase packed-bed operation. The anodic oxidation of sulfur dioxide (SO_2) in these cells can be involved in several electrochemical processes associated with the treatment of effluent waste gases, and possibly related to some energy conversion cycles.[3-9] The liquid-phase electrogenerative SO_2 oxidation which is considered further here has the potential advantage of being interfaced with various types of SO_2 preconcentration processes.[10,11]

However, the relatively small surface area of the commercial support available to us (Table II) has limited catalyst dispersion in our hybrid electrogenerative liquid-phase SO_2/O_2 cells. An increase in effective surface area of the packed-bed electrodes is needed to enhance performance.[12] At the same time, it is undesirable to have a pressure-drop increase for electrolyte flow through the packed-bed from any additional surface area (*e.g.*, activated-carbon bed).[13] While there have been other investigations into more efficient packed-bed electrodes for obtaining higher current densities,[14,15] these increases often are associated with surface-area increase and/or facilitation of the mass-transfer processes.

The approach adopted here for increasing the effective surface area of packed-bed electrodes for electrogenerative processing is to fabricate them with platinum electrocatalysts supported on large-surface-area carbon-black microporous structures and attached to relatively large graphite particles so that a bulk macroporous structure is maintained (Fig. 1a). The use of such a structure was suggested in earlier work by McIntyre and Phillips,[16] who fabricated this type of electrode for use in trickle-bed reactors for hydrogen peroxide production.[17] They used an inert polymer binder for carbon attachment as other workers such as Landi.[18] This general approach with operation in the electrogenerative mode allows adaption of large-surface-area carbon blacks widely used in gas-diffusion-electrode fabrication[19] to packed-bed-electrode application and to realization of flow-through-porous-electrode operation.[20] Heretofore, the large pressure-drop for electrolyte flow-through microporous beds and high contact resistance between small particles has limited the use of such catalysts. The attachment of the finer carbon-black-supported platinum electrocatalyst to larger graphite particles allows macroporosity to be compatible with enhanced active surface, with some limitations. The contact resistance of the packed beds also decreases in comparison with activated-carbon (or carbon-black) packed beds. Because of the larger bulk graphite-particle networks, commercially available active catalytic materials of different types also can be incorporated into the structure.

Despite their apparent advantages, applications of this type of electrocatalyst structure have been rare in the literature. Here, the results of applying these ESAP electrodes for electrogenerative oxidation of SO_2 are reported to illustrate their utility and potential applications. Mathematical

* Electrochemical Society Student Member.
** Electrochemical Society Active Member.